



# Anchoring black phosphorus quantum dots on molybdenum disulfide nanosheets: a 0D/2D nanohybrid with enhanced visible – and NIR – light photoactivity

Rongjuan Feng<sup>a</sup>, Wanying Lei<sup>b,c</sup>, Xinyu Sui<sup>b,c</sup>, Xinfeng Liu<sup>b</sup>, Xiaoying Qi<sup>b</sup>, Kun Tang<sup>d</sup>, Gang Liu<sup>b,\*</sup>, Minghua Liu<sup>a,c,\*</sup>

<sup>a</sup> CAS Key Laboratory of Nanosystem and Hierarchical Fabrication, CAS Center for Excellence in Nanoscience, National Center for Nanoscience and Technology, Beijing, 100190, PR China

<sup>b</sup> CAS Key Laboratory of Standardization and Measurement for Nanotechnology, CAS Center for Excellence in Nanoscience, National Center for Nanoscience and Technology, Beijing, 100190, PR China

<sup>c</sup> University of Chinese Academy of Sciences, Beijing, 100049, PR China

<sup>d</sup> Beijing Synchrotron Radiation Facility, Institute of High Energy Physics, Chinese Academy of Sciences, Beijing, 100049, PR China

## ARTICLE INFO

### Keywords:

Black phosphorus  
Molybdenum disulfide  
Visible light  
Near infrared light  
Photocatalysis

## ABSTRACT

The photocatalytic solar-to-chemical energy conversion by direct utilizing the full spectrum of sunlight is attracting a great deal of current attention. Black phosphorus (BP), a “rising star” of post-graphene two-dimensional (2D) nanomaterial, holds a unique advantage for this purpose on account of its tunable direct-bandgap for broadband absorption. In this work, for the first time, we anchor BP quantum dots (BPQDs) of  $\sim 4.2$  nm in size onto molybdenum disulfide (MoS<sub>2</sub>) nanosheets of  $\sim 3$  nm in thickness to create 0D/2D nanohybrids with various BP contents (5–20 wt %) via a facile and cost-effective grinding and sonicating approach. The as-prepared BPQDs/MoS<sub>2</sub> nanohybrids show enhanced photocatalytic performance towards methylene orange degradation in water under visible – and near – infrared (NIR) light illumination, respectively. Notably, 10 wt% BPQDs/MoS<sub>2</sub> nanohybrids with cyclability achieve the highest NIR – driven photoactivity ( $3 \times 10^{-2} \text{ min}^{-1}$ ), which is approximately 13 and 27 folds higher than that of individual BPQDs and MoS<sub>2</sub>, respectively. We demonstrate that the enhanced light absorption, the type – II band alignment, and the interfacial bonding and the spatial charge separation between well-dispersed BPQDs and MoS<sub>2</sub> synergetically enhance the photoactivity and photostability. This study may open avenues to create BP-based heterostructures functional in solar-to-chemical energy conversion and beyond.

## 1. Introduction

Ultrathin two-dimensional (2D) materials are currently attracting tremendous attention due to their unique physical, electronic, optical and chemical properties that are unattainable in their 3D counterparts [1–4]. The unprecedented physicochemical properties enable ultrathin 2D materials to be one versatile platform for the creation of multifunctional nanohybrids. For instance, in the areas of energy conversion and storage, 2D nanosheets-derived nanohybrids show potential applications ranging from solar cells to batteries and catalysis [5–8]. In view of direct utilizing clean, abundant and renewable solar energy, advanced materials that can harvest the full solar spectrum from UV to visible – and near – infrared (NIR) regions are highly desirable [9–15]. To date, studies focused on the solar-to-chemical energy conversion

utilizing NIR light that accounts for approximately 48% of the solar spectrum are rather limited [16,17].

Among a variety of 2D materials, black phosphorus (BP) is a “rising star” with a wide range of potential applications, such as electronics, optoelectronics, biomedicine, catalysis, energy storage and so on [18–20]. BP in a few- or mono-layer exhibits a layer-dependent direct-bandgap (0.3–2.1 eV) and high hole mobility up to  $\sim 1000 \text{ cm}^2 \text{ V}^{-1} \text{ s}^{-1}$  [21]. Accordingly, BP has emerged as an appealing candidate photocatalytic material with remarkable visible- and NIR-light responsivity [22–25]. Additionally, BP presents a puckered honeycomb structure with armchair- and zigzag-configurations along the x- and y-axial directions, respectively [22,26]. When the lateral sizes of ultrathin BP nanosheets are reduced to less than 20 nm, 0D BP quantum dots (BPQDs) are formed. In general, as compared with their 2D parental

\* Corresponding authors.

E-mail addresses: [liug@nanoctr.cn](mailto:liug@nanoctr.cn) (G. Liu), [liuminghua@nanoctr.cn](mailto:liuminghua@nanoctr.cn) (M. Liu).

<https://doi.org/10.1016/j.apcatb.2018.07.052>

Received 24 May 2018; Received in revised form 13 July 2018; Accepted 15 July 2018

Available online 17 July 2018

0926-3373/© 2018 Elsevier B.V. All rights reserved.

forms, QDs offer high absorption co-efficient, prominent edge and quantum confinement effects and facile hybridization with dissimilar materials [27,28]. Currently, research on BPQDs is predominantly focused on biomedicine and electronics [29–31], far less information is available regarding other areas like solar-driven photocatalysis that holds promise in the sustainable development of energy and environment. Apart from BP, another major class of 2D nanomaterials is molybdenum disulfide ( $\text{MoS}_2$ ), a typical transition metal disulfide featuring either indirect- (1.2 eV for bulk) or direct-bandgap (1.9 eV for monolayer) [28,32,33]. When designing high-performance photocatalysts, a rational combination of dissimilar semiconducting materials to form nanoscale heterojunctions is an effective way. The heterojunctions are expected to hold the complementary attributes and functionalities of the constituents and facilitate the spatial separation of photoexcited electron-hole pairs and so on [34,35].

In this work, for the first time, we prepared a 0D/2D nanohybrid by depositing ultrasmall BPQDs on ultrathin  $\text{MoS}_2$  nanosheets via a facile and cost-effective grinding and sonicating approach. In a range of BPQDs contents (5–20 wt%), BPQDs with an average size of  $\sim 4.2$  nm were anchored on the surface of  $\text{MoS}_2$  nanosheets of  $\sim 3$  nm in thickness. Compared with individual BPQDs and  $\text{MoS}_2$  nanosheets, the resulting BPQDs/ $\text{MoS}_2$  nanohybrids with an optimal BPQD content displayed enhanced photoactivity and photostability towards the degradation of a model dye methylene orange (MO) in water under visible- and NIR-light illumination, respectively. The underlying photocatalytic mechanisms were elucidated, highlighting the synergy of the light absorption enhancement, the type-II band alignment, the formation of interfacial bonds and the associated efficient charge separation across the interface between well-dispersed BPQDs and  $\text{MoS}_2$ .

## 2. Materials and methods

### 2.1. Chemicals

BP (> 99.998%) and  $\text{MoS}_2$  crystalline powders (> 99.998%) were purchased from Nanjing XFNANO Materials TECH Co., Ltd. Ammonium oxalate (AO, > 99%) and *p*-benzoquinone (PBQ, > 99%) were supplied by Acros. Tert-butyl alcohol (TBA, > 99.5%) and methyl orange (MO, > 99.5%) were purchased from Alfa Aesar. All reagents were of analytically pure grade and used without further purification. Milli-Q water (18 M $\Omega$  cm, Millipore) was used throughout this study.

### 2.2. Preparation of BPQDs/ $\text{MoS}_2$ nanohybrids

The BPQDs/ $\text{MoS}_2$  nanohybrids were synthesized through grinding, followed by agitated sonication in Milli-Q water. In detail,  $\text{MoS}_2$  and BP powders with target mass ratios were mixed and ground thoroughly. The resultant powders were dispersed into 50 mL Milli-Q water that was bubbled with argon to remove the dissolved oxygen, and sonicated in an ice bath for 8 h to construct BP/ $\text{MoS}_2$  nanohybrids. The BP/ $\text{MoS}_2$  hybrids were subsequently collected from the above suspension by centrifugation (15,000 rpm) and dried under vacuum. Herein, a series of BPQDs/ $\text{MoS}_2$  hybrids with different nominal BP mass contents (i.e., 5, 10, 15 and 20 wt%) were prepared. For comparison, both BPQDs and  $\text{MoS}_2$  nanosheets were also prepared by the above method.

### 2.3. Characterization

Transmission electron microscopy (TEM) imaging was taken on a Tecnai G<sup>2</sup> F20 U-TWIN microscopy with a 200 kV accelerating voltage. The energy dispersive X-ray (EDX) mapping was obtained using an accessory attached on TEM. High-angle annular dark-field (HAADF) scanning transmission electron microscopy (STEM) images were acquired on a JEOL JEM ARM 200 F instrument (Tokyo, Japan) equipped with a CEOS (Heidelberg, Germany) probe aberration corrector. Tapping-mode atomic force microscopy (AFM) images were obtained

by using a Dimension 3100 instrument (Veeco) with the samples deposited on a silicon wafer. Raman measurements were conducted using a LabRAM HR Evolution Raman spectroscopy system (HORIBA) with a 532 nm excitation laser at room temperature. The UV-vis spectra were recorded on a Shimadzu UV-2600 spectrometer. The diffuse reflectance UV-vis (DRUV-vis) spectra were recorded using a PerkinElmer Lambda-950 UV-vis spectrometer attached with an integrated sphere.  $\text{BaSO}_4$  was used as a reference. X-ray photoelectron spectroscopy (XPS) data were collected using an ESCALAB250XI electron spectrometer (VG, USA). X-ray absorption near-edge spectroscopy (XANES) spectra were recorded at 4B7A beamline of Beijing Synchrotron Radiation Facility (BSRF) of the Institute of High Energy Physics, Chinese Academy of Science. A Silicon Drifted Detector (SDD) was used to acquire data in partial fluorescence yield (PFY). Powder X-ray diffraction (XRD) patterns were acquired on a Shimadzu XRD-6000 diffractometer with Cu K $\alpha$  radiation ( $\lambda = 0.154178$  nm, 50 kV, 300 mA). The energy resolution at the P K-edge was close to 0.5 eV. All the XANES spectra were taken at room temperature. Solid-state  $^{31}\text{P}$ -nuclear magnetic resonance (NMR) analysis was carried out on a Bruker Avance III (600 MHz) spectrometer using a standard Bruker 4 mm double-resonance H-X MAS probe. The spectra of  $^{31}\text{P}$  were referenced externally to 85%  $\text{H}_3\text{PO}_4$  in aqueous solution ( $\delta = 0$  ppm). Steady state photoluminescence (PL) spectra were collected on a NanoLOG-TCSPC luminescence spectrophotometer with an excitation wavelength of 532 nm at room temperature. Femtosecond transient absorption (TA) measurements with a temporal resolution of  $\sim 130$  fs were performed using a commercial fs-TAS system (HELIOS, Ultrafast Systems).<sup>39</sup> Briefly, the 800 nm pulse from a Coherent Astrella regenerative amplifier (80 fs, 1 kHz, 2.5 mJ per pulse), seeded by a Coherent Vitara-s oscillator (35 fs, 80 MHz), was used to pump an optical parametric amplifier (Coherent, OperA Solo) to generate excitation pulse at 400 nm. The pump beam was chopped at 500 Hz with pump fluence at  $\sim 10 \mu\text{J cm}^{-2}$ , while a small fraction of the 800 nm output from the Astrella was fed to a sapphire crystal in the HELIOS for generating the white light continuum (WLC). A 750 nm short pass filter (SPF) was placed in the probe path before the sample to filter out the residual 800 nm in the WLC.

### 2.4. Photocatalytic performance and the detection of reactive species

The photoactivity of the as-prepared BPQDs/ $\text{MoS}_2$  nanohybrids was evaluated towards photodegradation of aqueous MO under visible- and NIR-light irradiation, respectively. Prior to light irradiation, 25 mg of the nanohybrids was thoroughly dispersed into an aqueous solution of MO (50 mL,  $5 \times 10^{-4}$  M) in a 150 mL beaker. Subsequently, the suspension was sonicated for 30 min and magnetically stirred in the dark for 60 min to ensure the complete adsorption – desorption equilibrium. A 300 W xenon lamp (Microsolar300, Beijing PerfectLight Science & Technology Co., Ltd) with a 420 nm and a 780 nm cut-off filter was used as the excitation source, respectively. During the illumination, the solution temperature was kept at room temperature. At certain time intervals, 3.0 mL aliquots were sampled and centrifuged at 15,000 rpm for 10 min to remove catalyst particulates. The photocatalytic activity was assessed by measuring the absorbance of the solution using a Shimadzu UV-2600 spectrometer at the maximum absorption wavelength (463 nm) for MO. To detect the major reactive intermediate species, AO, TBA and BPQ were selected as scavengers for the holes ( $\text{h}^+$ ), hydroxyl radicals ( $\cdot\text{OH}$ ), and superoxide radicals ( $\cdot\text{O}_2^-$ ), respectively. The detection of reactive species was similar to the procedure used for the MO degradation as described above, except introducing a target scavenger prior to adding the BPQDs/ $\text{MoS}_2$  catalyst powders. The respective concentration of AO, TBA, and PBQ is 10, 10, and 0.5 mM.

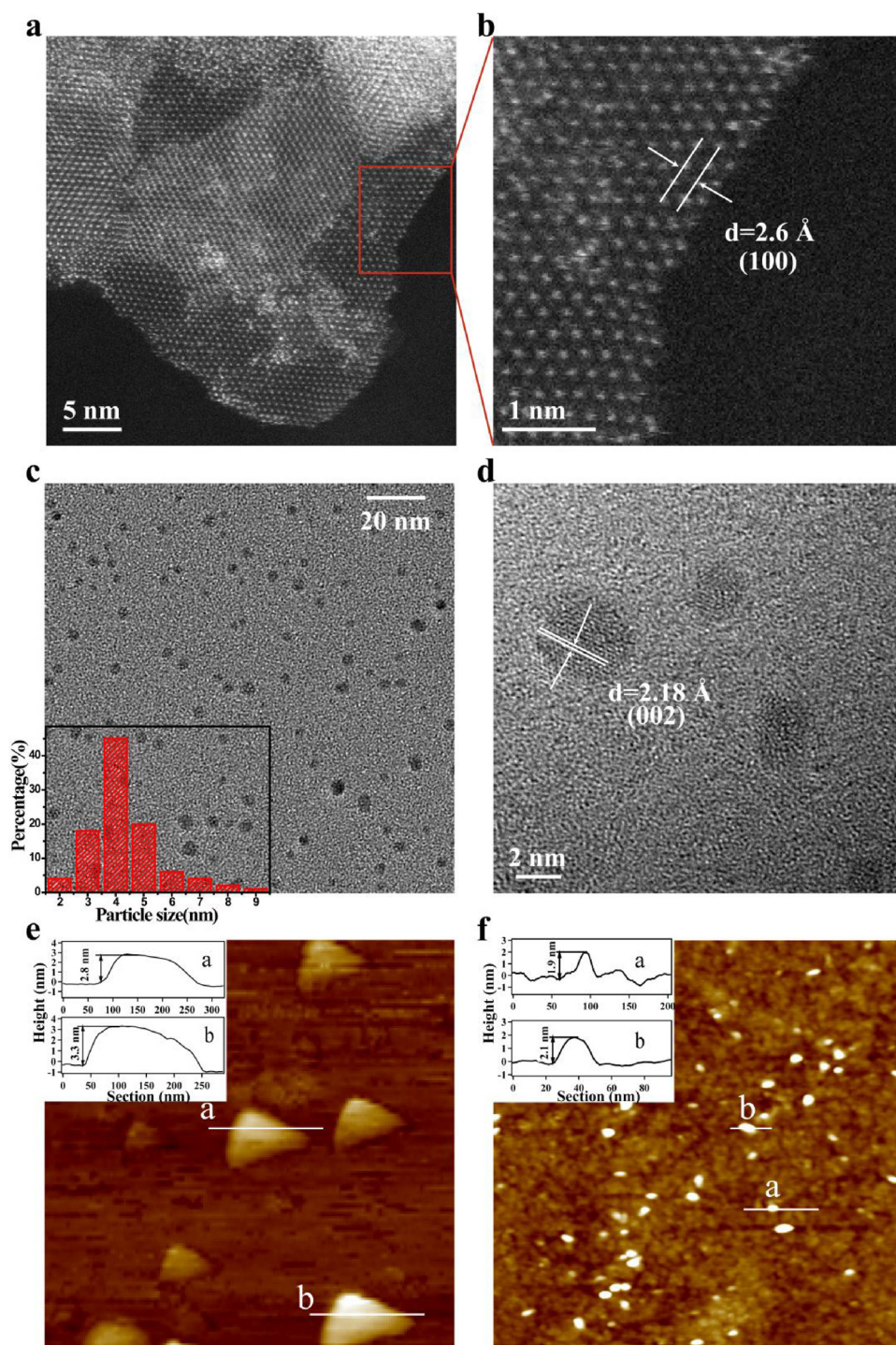


**Fig. 1.** Microscopic characterization of pristine MoS<sub>2</sub> nanosheets and BPQDs. (a) Atomically-resolved HAADF-STEM image of pristine MoS<sub>2</sub> nanosheets. (b) High-magnification HAADF-STEM image of the square in Fig. 1a, highlighting the Mo atom distribution along the edges. (c) Typical low-magnification TEM image of pristine BPQDs. Inset: the size distributions of pristine BPQDs. (d) Representative high-resolution TEM image of pristine BPQDs. (e) AFM image of MoS<sub>2</sub> nanosheets. Inset: height profiles corresponding to the lines drawn in the image. (f) Representative AFM image of BPQDs. Inset: height profiles corresponding to the lines drawn in the image.

### 3. Results and discussion

#### 3.1. Microscopic characterization

Fig. 1a shows a HAADF-STEM image of pristine MoS<sub>2</sub> nanosheets. The lateral size of these MoS<sub>2</sub> nanosheets is tens of nanometers. In Fig. 1b, a close look into pristine MoS<sub>2</sub> nanosheets reveals an interplanar spacing of 2.6 Å that is in accordance with that of (100) plane. Generally, the aberration-corrected STEM imaging contrast strongly depends on the atomic number (*Z*) of elements, with the contrast of HAADF imaging displaying a  $Z^{1.7}$  dependency. Herein, Mo atoms rather than S atoms are probed in the HAADF-STEM detection mode. Fig. 1b

exhibits Mo atoms along the edges of MoS<sub>2</sub> nanosheets. Fig. 1c shows a typical low-magnification TEM image of pristine BPQDs with an average lateral size of  $(4.2 \pm 1.2)$  nm. High-resolution TEM image in Fig. 1d illustrates that a well-resolved interplanar spacing of BPQDs is 2.18 Å, which is consistent with the *d*-spacing of (002). Tapping-mode AFM was employed to measure the thickness of the pristine MoS<sub>2</sub> nanosheets and BPQDs, as illustrated in Fig. 1e and 1f. And the corresponding height profiles are displayed in the insets of Fig. 1e and 1f. Based on a statistical analysis of 100 individual nanosheets, the average height of the pristine MoS<sub>2</sub> nanosheets is  $(3.0 \pm 0.4)$  nm that approximately corresponds to 3 atomic layers in thickness [36]. Likewise, the average thickness of BPQDs obtained by the statistical analysis of



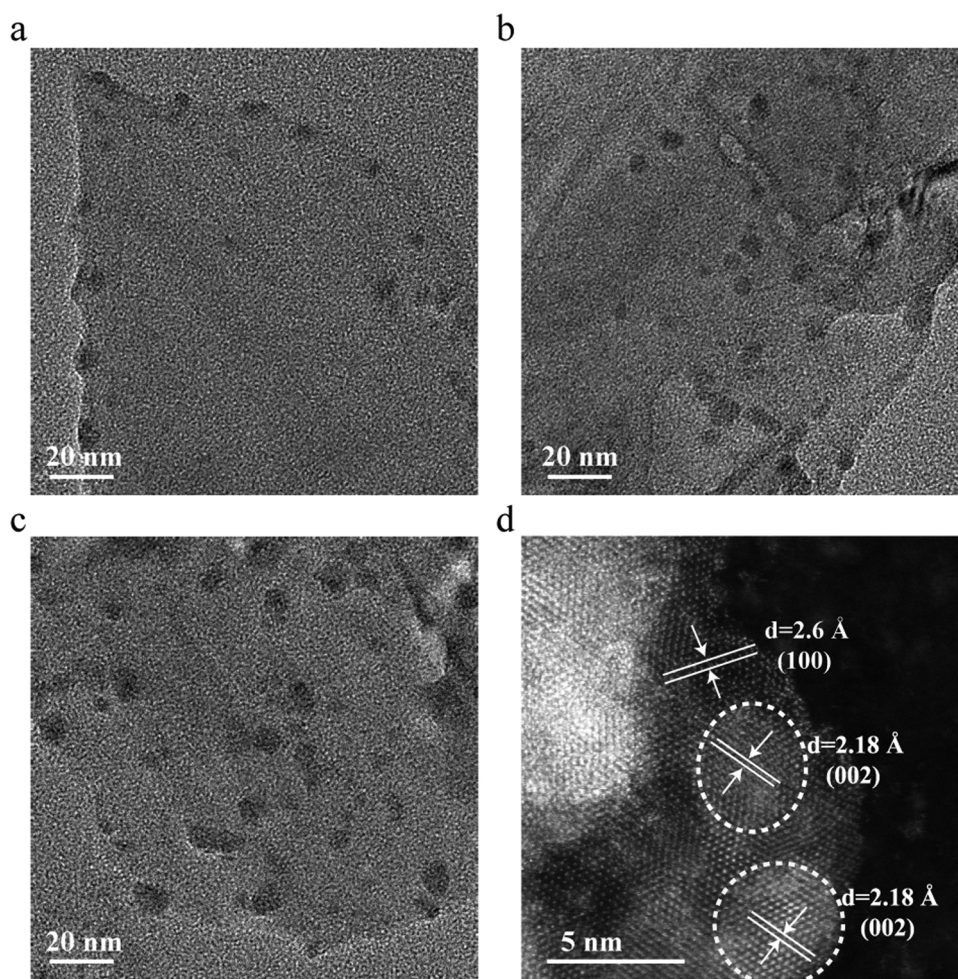


**Fig. 2.** Microscopic characterization of BPQDs/MoS<sub>2</sub> nanohybrids. Representative TEM images of (a) 5 wt% BPQDs/MoS<sub>2</sub>, (b) 10 wt% BPQDs/MoS<sub>2</sub> and (c) 15 wt% BPQDs/MoS<sub>2</sub>. (d) Atomically-resolved HAADF-STEM image of 10 wt% BPQDs/MoS<sub>2</sub>. White circles indicate the BPQDs. (For interpretation of the references to colour in this figure legend, the reader is referred to the web version of this article.)

100 BPQDs is  $(2.0 \pm 0.6)$  nm that is equal to  $(4 \pm 1)$  atomic layers. Fig. 2a and c show the TEM images of BPQDs/MoS<sub>2</sub> hybrids with different BP contents of 5–15 wt%. Apparently, the density of the BPQDs increases with the increasing BP content. As shown in Fig. 2a and b, the pseudo-spherical BPQDs are well dispersed on the terraces as well as the edges of the MoS<sub>2</sub> nanosheets for the relatively low BPQDs contents of 5–10 wt%. Notably, some BPQDs tend to distribute along the edges of the MoS<sub>2</sub> nanosheets. Further increasing the BP content up to 15 wt% induces a tendency of self-aggregation (Fig. 2c). In the case of 20 wt% BPQDs/MoS<sub>2</sub>, Fig. S1 in the Supporting Information illustrates significant particle aggregation. The atomically-resolved HAADF-STEM imaging of the BPQDs for 10 wt% BPQDs/MoS<sub>2</sub> in Fig. 2d presents lattice fringes of 2.6 and 2.18 Å, which can be ascribed to the (100) plane of MoS<sub>2</sub> and the (002) plane of BP, respectively. TEM-based EDX was conducted to show the actual compositions (Fig. S2) and corresponding element distribution (Fig. S3) of BPQDs/MoS<sub>2</sub> nanohybrids.

### 3.2. Spectroscopic characterization

Fig. 3a shows the Raman spectra of BPQDs, MoS<sub>2</sub> nanosheets and BPQDs/MoS<sub>2</sub> nanohybrids. As for pristine BPQDs, the peaks located at 363, 440, and 467 cm<sup>-1</sup> were assigned to out-of-plane phonon mode A<sub>g</sub><sup>1</sup>, in-plane phonon mode B<sub>g</sub>, and in-plane phonon mode A<sub>g</sub><sup>2</sup>, respectively [37,38]. For pristine MoS<sub>2</sub> nanosheets, two prominent peaks at 383 and 408 cm<sup>-1</sup> are observed, which are assigned to E<sub>2g</sub><sup>1</sup> and A<sub>1g</sub> modes, respectively [35]. Notably, the frequency difference between

E<sub>2g</sub><sup>1</sup> and A<sub>1g</sub> is about 25 cm<sup>-1</sup>, which suggests the thickness of the as-prepared MoS<sub>2</sub> nanosheets is within few-layers [39,40]. In comparison with pristine MoS<sub>2</sub> nanosheets, no obvious shift was observed for the peaks in BPQDs/MoS<sub>2</sub> hybrids for the relatively low BPQDs contents of 5–10 wt%. In the case of 20 wt% BPQDs/MoS<sub>2</sub>, the A<sub>g</sub><sup>2</sup> peak exhibits a blue shift compared with that of BPQDs whereas the E<sub>2g</sub><sup>1</sup> and A<sub>1g</sub> peaks present a red shift compared with that of MoS<sub>2</sub>, suggesting possible electron transfer across the BPQDs/MoS<sub>2</sub> interface [35]. The crystalline structures of MoS<sub>2</sub> nanosheets, BPQDs and BPQDs/MoS<sub>2</sub> nanohybrids were also verified by XRD patterns. As shown in Fig. S4, BPQDs/MoS<sub>2</sub> nanohybrids with different BP contents exhibit comparable hexagonal structure (JCPDS 37-1492) with respect to pristine MoS<sub>2</sub> [41]. Besides, BPQDs/MoS<sub>2</sub> nanohybrids exhibit characteristic diffraction peaks of BP. The above XRD results confirm the co-existence of both BP and MoS<sub>2</sub> crystallites. To investigate the optical absorption properties of the as-prepared samples, UV–vis spectroscopy is employed. Fig. 3b shows the UV–vis spectra of MoS<sub>2</sub> nanosheets and BPQDs/MoS<sub>2</sub> nanohybrids. Both MoS<sub>2</sub> nanosheets and BPQDs/MoS<sub>2</sub> hybrids display four characteristic absorption bands. The peaks at 610 nm (B-exciton) and 670 nm (A-exciton) result from the K point of the Brillouin zone [32,42]. The distinct peaks located at 395 and 450 nm could be assigned to the direct transition from the valence band (VB) to the conduction band (CB) [43,44]. Notably, the BPQDs/MoS<sub>2</sub> nanohybrids show enhanced light absorption in the range of 300–800 nm, and the absorption intensity increases with increasing BP content. Fig. S5 compares the light absorption edges of MoS<sub>2</sub> and BPQDs, which were

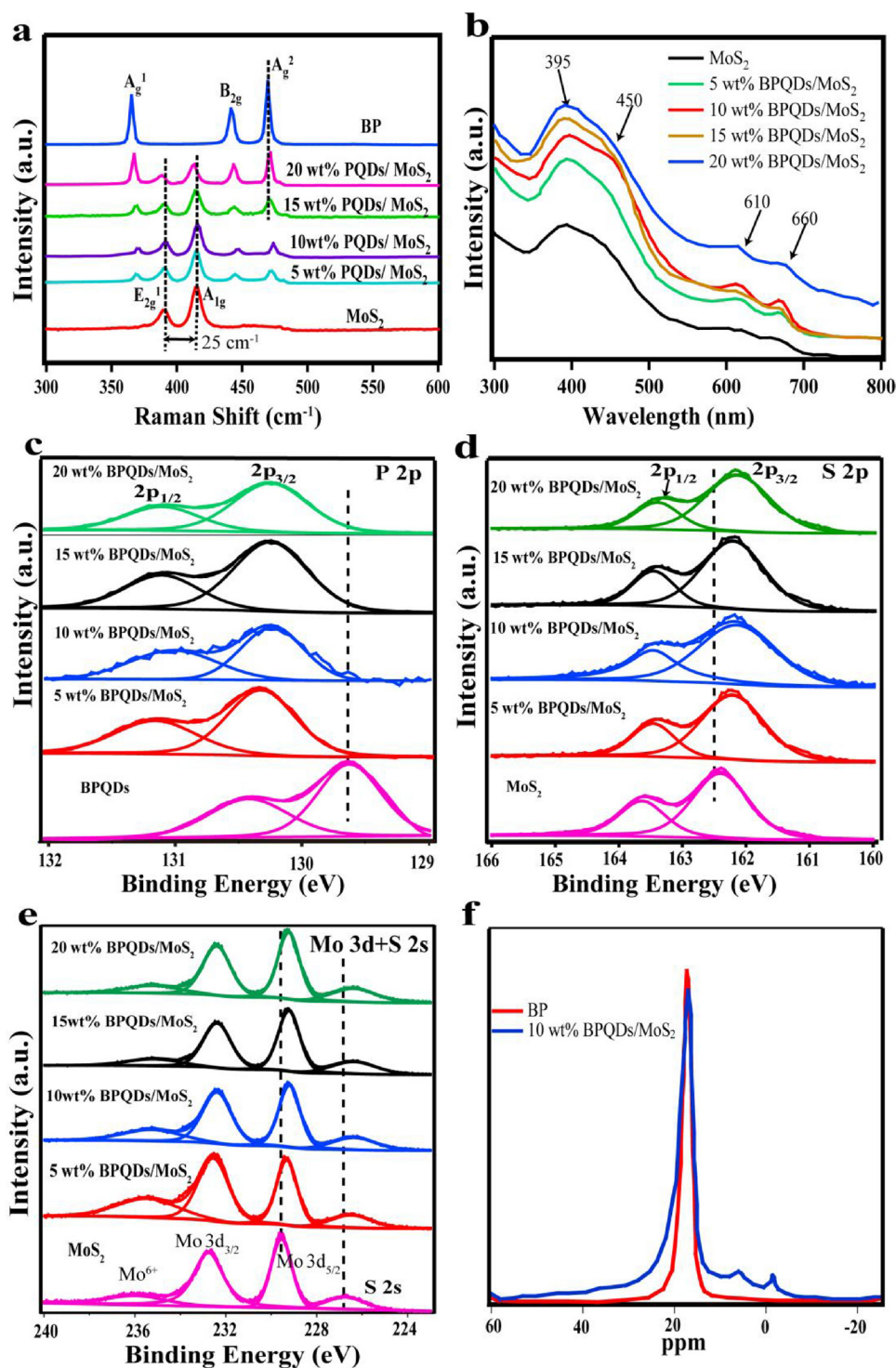


**Fig. 3.** Spectroscopic characterization of pristine MoS<sub>2</sub> nanosheets, BPQDs and BPQDs/MoS<sub>2</sub> nanohybrids. (a) Micro-Raman spectra of MoS<sub>2</sub> nanosheets, BPQDs and BPQDs/MoS<sub>2</sub> hybrids. (b) UV-vis spectra of MoS<sub>2</sub> nanosheets and BPQDs/MoS<sub>2</sub> nanohybrids. High-resolution XPS core-level spectra of (c) P 2p, (d) S 2p, and (e) Mo 3d and S 2s. (f) Solid-state <sup>31</sup>P-NMR spectra of pristine BPQDs and 10% BPQDs/MoS<sub>2</sub>.

measured to be respective 730 and 803 nm. Thereby, the bandgap ( $E_g$ ) is determined to be 1.7 and 1.54 eV for MoS<sub>2</sub> nanosheets and BPQDs, respectively. The DRUV-vis spectra of MoS<sub>2</sub>, BPQDs, and 10 wt% BPQDs/MoS<sub>2</sub> hybrids are depicted in Fig. S6. In comparison with MoS<sub>2</sub>, 10 wt% BPQDs/MoS<sub>2</sub> hybrids exhibit enhanced absorption, in particular in the NIR regime from 800 to 1400 nm. To further probe the electron transfer and associated interfacial bonding in the BPQDs/MoS<sub>2</sub> nanohybrids, we conducted XPS measurements. Fig. 3c displays the

high-resolution XPS spectra of the P 2p core level. The peaks located at 130.2 and 131 eV can be assigned to the P 2p<sub>3/2</sub> and P 2p<sub>1/2</sub>, respectively. Notably, the P 2p<sub>3/2</sub> peak for BPQDs/MoS<sub>2</sub> nanohybrids shows a positive shift (ca. 0.6 eV) in comparison with that of pristine BPQDs. Fig. 3d shows the S 2p spectra for MoS<sub>2</sub> nanosheets and BPQDs/MoS<sub>2</sub> hybrids. As for MoS<sub>2</sub> nanosheets, the S 2p core level displays a S 2p<sub>1/2</sub> and S 2p<sub>3/2</sub> doublet at 163.6 and 162.4 eV, respectively [45]. Apparently, the S 2p<sub>3/2</sub> peak presents a negative shift (ca. 0.3 eV) relative to



that of MoS<sub>2</sub> nanosheets. Fig. 3e exhibits the Mo 3d and S 2s spectra of MoS<sub>2</sub> nanosheets and BPQDs/MoS<sub>2</sub> nanohybrids. For MoS<sub>2</sub> nanosheets, two peaks located at 232.7 and 229.2 eV are assigned to Mo<sup>4+</sup> 3d<sub>3/2</sub> and Mo<sup>4+</sup> 3d<sub>5/2</sub>, respectively [46]. The Mo<sup>4+</sup> 3d<sub>5/2</sub> peak for BPQDs/MoS<sub>2</sub> nanohybrids shows a negative shift of ca. 0.3 eV with respect to that of MoS<sub>2</sub> nanosheets. The peak at 226.7 eV can be assigned to the S 2s peak in typical sulfides. Like the S 2p peaks, the S 2s peak shows a negative shift of 0.3 eV relative to that of MoS<sub>2</sub> nanosheets as well. A relatively weak peak at 259.5 eV is due to the Mo<sup>6+</sup> species [47]. Based on the above XPS results, we can conclude that the electron transfer occurs from BPQDs to MoS<sub>2</sub> nanosheets, indicating the interfacial bond formation upon their coupling [48]. Fig. S7 depicts the XPS VB spectra of pristine MoS<sub>2</sub> nanosheets and BPQDs. The VB maximum of MoS<sub>2</sub> nanosheets and BPQDs is 1.54 and 0.76 eV, respectively. In conjunction with the aforementioned bandgap values, the CB minimum of MoS<sub>2</sub> and BPQDs is calculated to be −0.16 and −0.78 eV (vs NHE), respectively. It is well-known that the K-edge features of XANES are very sensitive to the chemical environment around the X-ray absorbing atom [49]. Herein, the absorption at the P K-edge reflects the electronic transitions from the P 1s core-level into the empty P 3p level, which in turn provides information concerning the electronic interactions between BPQDs and MoS<sub>2</sub>. Fig. S8 shows that the peak position increases by ~0.6 eV from 2144.5 eV (BPQDs) to 2145.1 eV (10 wt% BPQDs/MoS<sub>2</sub> nanohybrids). The above results reflect that some of the BP atoms in the BPQDs/MoS<sub>2</sub> nanohybrids are in a special chemical environment in comparison with those of pristine BPQDs and charge transfer occurs from BPQDs to MoS<sub>2</sub>. The results of the P K-edge XANES are consistent with the aforementioned XPS analysis. To further prove the interactions between BPQDs and MoS<sub>2</sub> nanosheets, solid-state <sup>31</sup>P-NMR measurements of pristine BPQDs and 10% BPQDs/MoS<sub>2</sub> hybrid were carried out. As presented in Fig. 3f, only one peak at 17.3 ppm appears in the spectrum of BPQDs. In contrast, 10% BPQDs/MoS<sub>2</sub> nanohybrid display three peaks centered at 17, 6, and −1.4 ppm, respectively. The peak around 17 ppm is assigned to pristine BPQDs. The new peaks at 6 and −1.4 ppm are ascribed to the P-S and P-Mo bonds in the BPQDs/MoS<sub>2</sub> nanohybrids [50]. In summary, the results with a combination of XPS, XANES and NMR demonstrate the interfacial bonding between BPQDs and MoS<sub>2</sub>. As illustrated in the following sections, the interfacial P-S and P-Mo bonds in the BPQDs/MoS<sub>2</sub> nanohybrids benefits not only photoexcited charge transfer and photoactivity, but also photostability.

### 3.3. Photocatalytic property

The photocatalytic activities of MoS<sub>2</sub>, BPQDs, and BPQDs/MoS<sub>2</sub> hybrids were evaluated towards MO degradation under visible- and NIR-light irradiation, respectively. To evaluate the photoactivity quantitatively, the reaction rate constants were calculated on the basis of the Langmuir–Hinshelwood kinetics. For the blank experiment without photocatalysts (i.e., photolysis), MO degradation under either visible- or NIR-light illumination is negligible (Fig. S9). As shown in Fig. 4a, all the BPQDs/MoS<sub>2</sub> hybrids show greater photoactivity than either individual MoS<sub>2</sub> nanosheets or BPQDs under visible light illumination. The photoactivity increases with increasing BP content from 5% to 10 wt%. However, further increasing in BP content larger than 10 wt% decreases the photoactivity, probably due to the aforementioned partial self-aggregation of BPQDs for 15% wt% BPQDs/MoS<sub>2</sub> and 20 wt% BPQDs/MoS<sub>2</sub>. Herein, 10 wt% BPQDs/MoS<sub>2</sub> presents the greatest reaction rate constant of  $5.2 \times 10^{-2} \text{ min}^{-1}$ , which is 15.7 and 3.8 times larger than that of pristine MoS<sub>2</sub> nanosheets ( $3.3 \times 10^{-3} \text{ min}^{-1}$ ) and BPQDs ( $1.35 \times 10^{-2} \text{ min}^{-1}$ ), respectively. Further, the highest reaction rate constant of  $5.2 \times 10^{-2} \text{ min}^{-1}$  achieved by 10 wt% BPQDs/MoS<sub>2</sub> outperforms typical MoS<sub>2</sub>-based photocatalysts and other types of photocatalysts reported in the literature (Table S1). The corresponding UV-vis spectral changes of MO solutions photocatalyzed by 10 wt% BPQDs/MoS<sub>2</sub> as a function of illumination time are shown in Fig. S10a. In order to identify the major

active species responsible for MO degradation, control experiments with a few scavengers were carried out. By adding respective AO, TBA, and PBQ into the reaction solutions, the major active species in the degradation process can be revealed. Fig. 4b displays that the MO conversion by 10 wt% BPQDs/MoS<sub>2</sub> nanohybrids is 92% after 40 min without scavengers under visible light illumination. Nevertheless, the degradation efficiency of MO is reduced to 24% in the presence of AO. In contrast, negligible photocatalytic efficiency change was observed by adding TBA. And slightly decreased photoactivity was observed with the addition of PBQ in comparison with AO. The above results suggest that h<sup>+</sup> rather than •OH and •O<sub>2</sub><sup>−</sup> is the major active species responsible for MO degradation. To investigate the photostability of the BPQDs/MoS<sub>2</sub> nanohybrids, cyclability test was performed under identical conditions. After four cycles (8 h) of MO photodegradation, the apparent photocatalytic efficiency of 10 wt% BPQDs/MoS<sub>2</sub> nanohybrids still remains over 86%, as displayed in Fig. 4c. Likewise, under NIR-light illumination the photocatalytic activities of BPQDs/MoS<sub>2</sub> nanohybrids are enhanced in comparison with MoS<sub>2</sub> and BPQDs (Fig. 4d). Again, 10 wt% BPQDs/MoS<sub>2</sub> nanohybrids show the best performance. The corresponding UV-vis spectral changes of MO solutions are shown in Fig. S10b. The degradation rate is determined to be  $3 \times 10^{-2} \text{ min}^{-1}$ , which is approximately 27 and 13 times higher than that of pristine MoS<sub>2</sub> nanosheets ( $1.1 \times 10^{-3} \text{ min}^{-1}$ ) and BPQDs ( $2.3 \times 10^{-3} \text{ min}^{-1}$ ), respectively. The NIR light-driven photoactivity of 10 wt% BPQDs/MoS<sub>2</sub> outperforms that of some reported photocatalysts (Table S1). For 10 wt% BPQDs/MoS<sub>2</sub> hybrids, it can be seen that the photocatalytic degradation rate is largely inhibited with the addition of AO (Fig. 4e). In contrast, adding either PBQ or TBA induce much less effects, indicating h<sup>+</sup> is a predominant active species. As for photostability, the photocatalytic efficiency of 10 wt% BPQDs/MoS<sub>2</sub> nanohybrids only slightly decreases even after four cyclings (Fig. 4f). To examine the morphology and structure of 10 wt% BPQDs/MoS<sub>2</sub> nanohybrids after the photocatalytic reaction, TEM and Raman measurements were performed. No significant morphological changes (Fig. S11) and no obvious peak shifts for the major Raman bands are observed (Fig. S12). The above results demonstrate that 10 wt% BPQDs/MoS<sub>2</sub> nanohybrids are an efficient visible- and NIR-light responsive photocatalyst with cyclability.

### 3.4. Photocatalytic mechanisms of BPQDs/MoS<sub>2</sub> hybrids

PL is an efficient technique to probe the efficiency of photoexcited electron-hole recombination. As shown in Fig. 5a, the steady-state PL spectrum of pristine MoS<sub>2</sub> nanosheets shows a strong A exciton peak at 657 nm under the excitation wavelength of 532 nm at room temperature, which results from the high recombination of electron-hole pairs [51]. The intensity of this emission peak for 10 wt% BPQDs/MoS<sub>2</sub> hybrids decreases remarkably as compared to pure MoS<sub>2</sub> nanosheets, indicating that the coupling of BPQDs and MoS<sub>2</sub> nanosheets could facilitate the interfacial charge transfer via interfacial bonding and thus hinder the recombination of electrons and holes to promote photoactivity. The underlying charge carrier dynamics in real time is probed with femtosecond TA spectroscopy. The evolution of the TA spectra for pristine MoS<sub>2</sub> and 10 wt% BPQDs/MoS<sub>2</sub> as a function of delay time is depicted in Fig. 5b and c. As shown in Fig. 5b, ground state bleach (GSB) around 612 and 667 nm (denoted as PB-B and PB-A, respectively) are observed, in agreement with the absorption data by UV-vis spectrum of MoS<sub>2</sub>. There are two photoinduced absorption (PIA, positive ΔA) bands located at both sides of PB bands [39,52], which are attributed to photoinduced refractive index changes as shown in Fig. 5b. Upon 400 nm excitation, the TA spectra recorded for 10 wt% BPQDs/MoS<sub>2</sub> hybrids share comparable signals of MoS<sub>2</sub> alone, albeit the signal magnitude is significantly enlarged. The greater signal intensity implies that more charge carriers are generated in 10 wt% BPQDs/MoS<sub>2</sub> hybrids. The decay profiles probed at exciton A (667 nm) resonance region was studied to evaluate the decay kinetics of MoS<sub>2</sub> and 10 wt% BPQDs/

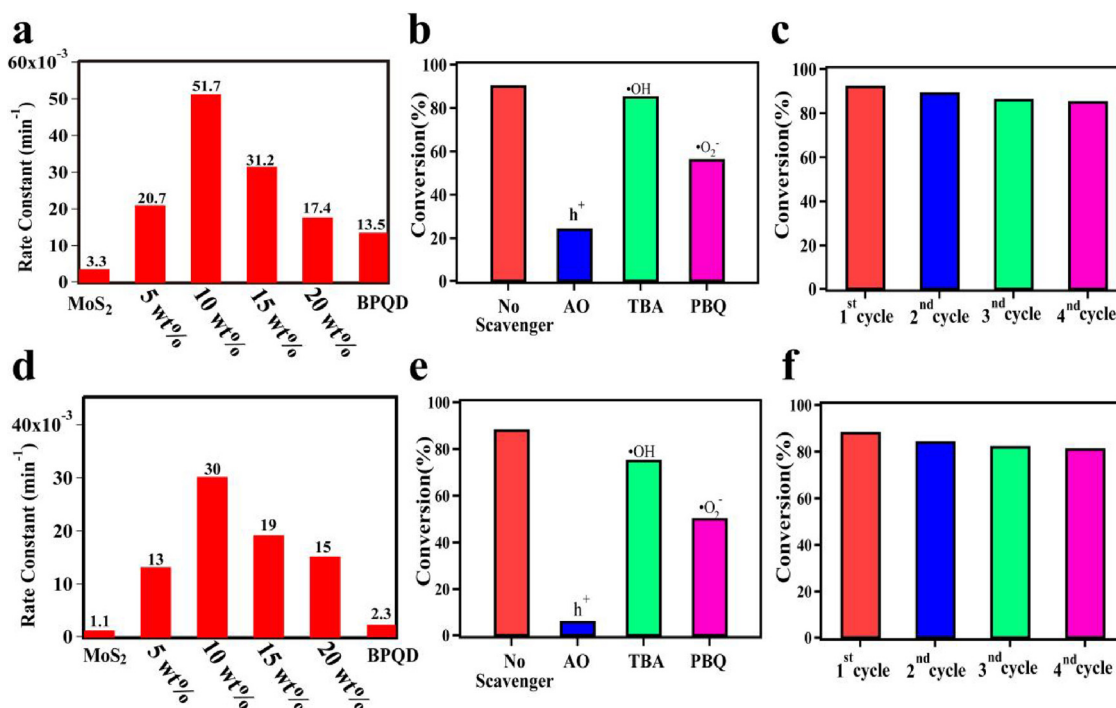


**Fig. 4.** Photocatalytic property evaluation. (a) Photoactivities of MoS<sub>2</sub> nanosheets, BPQDs and BPQDs/MoS<sub>2</sub> nanohybrids for MO degradation under visible – light illumination. (b) Control experiments in the presence of various scavengers over 10 wt% BPQDs/MoS<sub>2</sub> hybrids. (c) Recycling runs of 10 wt% BPQDs/MoS<sub>2</sub> hybrids for MO photodegradation under visible – light illumination. (d) Photoactivities of MoS<sub>2</sub> nanosheets, BPQDs and BPQDs/MoS<sub>2</sub> hybrids for MO degradation under NIR – light illumination. (e) Control experiments in the presence of various scavengers over 10 wt% BPQDs/MoS<sub>2</sub> hybrids. (f) Recycling runs of 10 wt% BPQDs/MoS<sub>2</sub> hybrids for MO photodegradation under NIR – light illumination.

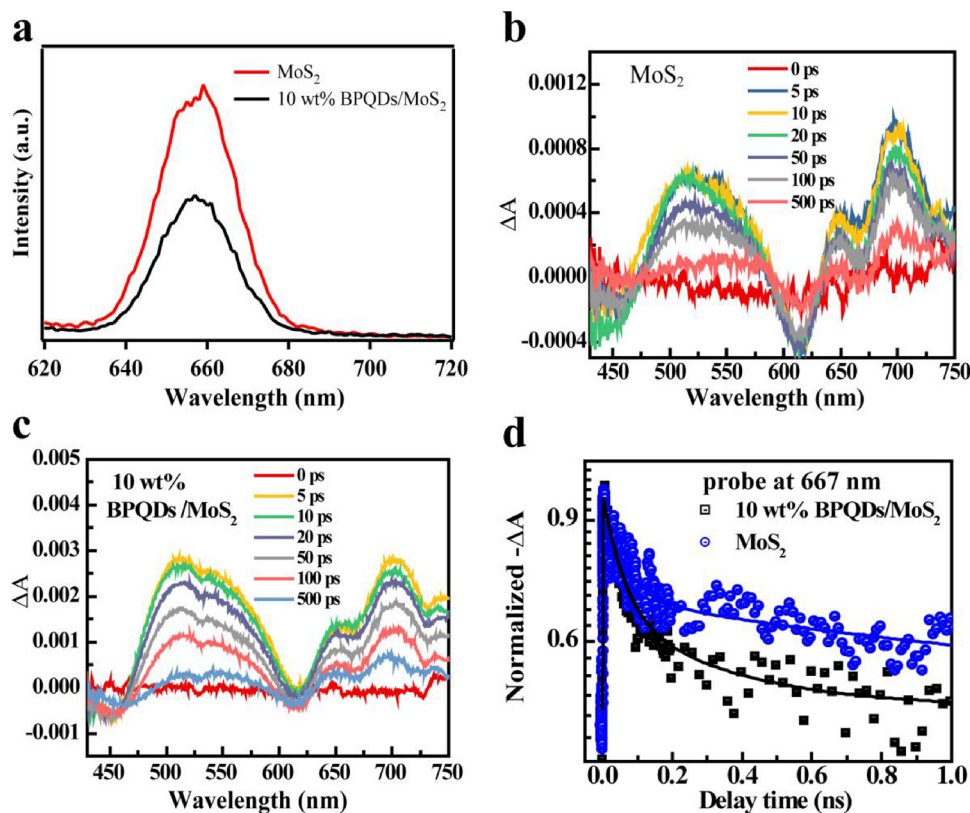


**Fig. 5.** Steady-state PL and TA spectroscopic characterization. (a) The room-temperature steady-state PL spectra of MoS<sub>2</sub> nanosheets and 10 wt% BPQDs/MoS<sub>2</sub> hybrids under light excitation at 532 nm. TA spectra of (b) MoS<sub>2</sub> and (c) 10 wt% BPQDs/MoS<sub>2</sub> hybrids under 400 nm light irradiation. (d) Normalized TA profiles observed at 667 nm.

MoS<sub>2</sub> hybrids as shown in Fig. 5d. The decay profiles were fitted with a bi-exponential decay function and the fitting parameters are summarized in Table S2. Decay time  $\tau_1$  and  $\tau_2$  for pristine MoS<sub>2</sub> nanosheets ( $70 \pm 10$  and  $1800 \pm 300$  ps, respectively) and BPQDs/MoS<sub>2</sub> hybrids ( $60 \pm 10$  and  $330 \pm 60$  ps, respectively) were extracted. The fast decay time  $\tau_1$  with tens of picoseconds was attributed to electron trapping by surface states near the CB, and the slow decay time  $\tau_2$  with hundreds of picoseconds was originated from the exciton recombination process [53]. Compared with pure MoS<sub>2</sub> nanosheets, the slow decay time constant  $\tau_2$  decreases, suggesting the presence of ultrafast charge transfer in 10 wt% BPQDs/MoS<sub>2</sub> hybrids. In fact, efficient charge transfer in the hybrids can suppress charge recombination process. Based on the steady-state PL and ultrafast TA results, we conclude that the combination of BPQDs and MoS<sub>2</sub> nanosheets can dramatically increase electron–hole separation efficiency and enhance the photoactivity.

In general, a typical semiconductor-based photocatalytic process comprises the following three steps. First, light illumination induces electron transition from VB to CB, thereby generating electron–hole pairs. Second, the photoexcited electrons and holes transfer to the surface. Third, they trigger the reduction or oxidation reactions, respectively. However, the electron–hole pairs tend to recombine and dissipate the input energy in the form of heat or emitted light. One of the efficient strategies to retard the recombination of electron–hole pairs is to construct nanoscale heterojunctions. Herein, we anchor OD BPQDs with an average size of  $\sim 4.2$  nm onto 2D MoS<sub>2</sub> nanosheets with an average thickness of  $\sim 3$  nm to form a typical type–II hybrid, which is expected to facilitate the separation of the electron–hole pairs and charge-carrier transfer [54,55]. Based on the CB and VB edge positions, the schematic diagrams for the improved photoactivity of the BPQDs/MoS<sub>2</sub> hybrids towards MO degradation under respective visible– and NIR–light illumination are depicted in Fig. 6. Under visible light illumination (Fig. 6a), both MoS<sub>2</sub> and BPQDs could generate electron–hole pairs. In detail, the photoexcited electrons in the CB of BPQDs could rapidly migrate to the CB of MoS<sub>2</sub> since the CB maximum ( $-0.78$  eV) of BPQDs is more negative than that ( $-0.16$  eV) of MoS<sub>2</sub>, and at the same time the photogenerated holes in the VB of MoS<sub>2</sub> could transfer to BPQDs. Namely, the suitable band edges of MoS<sub>2</sub> and BPQDs ensure that effective photoexcited electrons transfer occurs across the interface of the heterojunction, which results from the interfacial bonding in the hybrids. In the current study, the results of Raman, XPS, XANES and NMR confirm the intimate interactions between well-dispersed BPQDs and MoS<sub>2</sub> nanosheets. As a result, the spatial charge transfer retards the recombination of electron–hole pairs, resulting in improved photocatalytic activities as illustrated in Fig. 6a. The photocatalytic mechanism by BPQDs/MoS<sub>2</sub> nanohybrids under NIR-light illumination is shown in Fig. 6b. As mentioned above, the CB and VB of BPQDs is *ca.*

$-0.78$  and  $0.76$  eV vs. NHE, respectively. Thus, the BPQDs are responsive to the NIR-light excitation and then generate electron–hole pairs in the CB and VB, respectively. Although the photoexcited holes in the VB of BPQDs are suitable for MO degradation, pristine BPQDs show a negligible photoactivity due to the rapid recombination of photo-generated electron–hole pairs. However, in the BPQDs/MoS<sub>2</sub> hybrids, the photoexcited electrons in BPQDs are efficiently injected into MoS<sub>2</sub> nanosheets owing to the lower work function of MoS<sub>2</sub> ( $5.74$  eV) [56]. Accordingly, BPQDs/MoS<sub>2</sub> nanohybrids synergistically promote the charge separation as well as photoactivity. The roles of detected reactive species in the photocatalytic processes are rationalized as following. The electrons in the CB of BPQDs could react with O<sub>2</sub> adsorbed onto the surface of BPQDs/MoS<sub>2</sub> hybrids because the CB edge potential of BPQDs ( $-0.78$  eV) is more negative than the potential of O<sub>2</sub>/·O<sub>2</sub><sup>−</sup> ( $-0.33$  eV) [57], while the electrons in the CB of MoS<sub>2</sub> cannot react with O<sub>2</sub> to form active ·O<sub>2</sub><sup>−</sup> species in the photoexcited charge migration process in the hybrids. Therefore, the minor effect of active ·O<sub>2</sub><sup>−</sup> species was observed in the photocatalytic process since most photoexcited electrons will effectively transfer from the CB of BPQDs to the CB of MoS<sub>2</sub> in the hybrids, which is confirmed by the above trapping experiments. On the other hand, the holes left behind in the VB of BPQDs could not directly oxidize OH<sup>−</sup> or H<sub>2</sub>O to form ·OH, as the VB edge potential of BPQDs ( $+0.76$  eV) is more negative than the potentials of ·OH/H<sub>2</sub>O ( $+2.68$  eV) and ·OH/OH<sup>−</sup> ( $+1.99$  eV) [58]. In addition, the active ·OH species plays a minor role in promoting photocatalytic reaction, confirmed using TBA as a scavenger. Subsequently, the photogenerated holes collected in BPQDs can diffuse to the hybrid surface and directly oxidize organic pollutants due to their high oxidation potentials. In short, photogenerated holes are the primary active species responsible for the observed photocatalytic performance, while the enhanced photoactivity is attributed to the efficient charge separation driven by the type–II band alignment and interactions between MoS<sub>2</sub> and BPQDs.

#### 4. Conclusions

In summary, OD/2D mixed-dimensional BPQDs/MoS<sub>2</sub> nanohybrids are successfully fabricated by depositing BPQDs of  $\sim 4.2$  nm in size onto MoS<sub>2</sub> nanosheets of  $\sim 3$  nm in thickness through a facile and cost-effective grinding and sonication approach. The as-prepared BPQDs/MoS<sub>2</sub> nanohybrids exhibit enhanced photocatalytic performance towards MO degradation in water under visible– and NIR–light illumination, respectively. Under visible light illumination, in a range of BP contents (5–20 wt%), the highest photoactivity in terms of the reaction rate constant ( $5.2 \times 10^{-2} \text{ min}^{-1}$ ) is achieved by 10 wt% BPQDs/MoS<sub>2</sub> hybrids, which is 15.7 and 3.8 times larger than that of individual BPQDs and MoS<sub>2</sub> nanosheets, respectively. Under NIR light

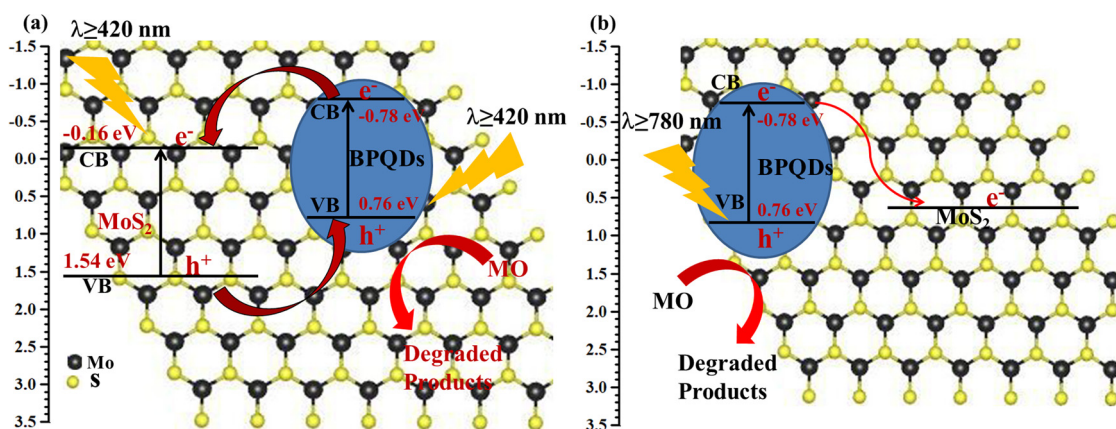


Fig. 6. Schematic diagrams of photocatalytic mechanisms for BPQDs/MoS<sub>2</sub> nanohybrids under (a) visible– and (b) NIR–light illumination, respectively. (For interpretation of the references to colour in this figure legend, the reader is referred to the web version of this article.)



illumination, 10 wt% BPQDs/MoS<sub>2</sub> hybrids achieve the greatest photoactivity ( $3 \times 10^{-2} \text{ min}^{-1}$ ), which is 13 and 27 folds higher than that of respective BPQDs and MoS<sub>2</sub>. It is found that photoexcited holes are major active species under either visible- or NIR-light illumination. The enhanced photoactivity for the BPQDs/MoS<sub>2</sub> hybrids could be ascribed to the enhanced optical absorption, the type-II band alignment, the promoted photogeneration of electron-hole pairs, and the efficient charge transfer across the interface from well-dispersed BPQDs to MoS<sub>2</sub> nanosheets. In particular, the intimate contact and associated interfacial P-S and P-Mo bonds between BPQDs and MoS<sub>2</sub> nanosheets play a crucial role in enhancing the photoactivity as well as photostability. This work has broad implications in the design and synthesis of a range of BP-based hybrid nanostructures functional in solar-to-chemical energy conversion, among others.

## Acknowledgments

This work was supported by National Natural Science Foundation of China (Nos. 91427302 and 51772058), Strategic Priority Research Program of the Chinese Academy of Sciences (No. XDB12020200).

## Appendix A. Supplementary data

Supplementary material related to this article can be found, in the online version, at doi:<https://doi.org/10.1016/j.apcatb.2018.07.052>.

## References

- [1] L. Dai, X. Feng, Z. Liu, H. Zhang, Two-dimensional materials: a powerful platform for energy applications, *ChemNanoMat* 3 (2017) 338–339.
- [2] C. Tan, X. Cao, X.J. Wu, Q. He, J. Yang, X. Zhang, J. Chen, W. Zhao, S. Han, G.H. Nam, M. Sindoro, H. Zhang, Recent advances in ultrathin two-dimensional nanomaterials, *Chem. Rev.* 117 (2017) 6225–6331.
- [3] X.D. Duan, C. Wang, A.L. Pan, R.Q. Yu, X.F. Duan, Two-dimensional transition metal dichalcogenides as atomically thin semiconductors: opportunities and challenges, *Chem. Soc. Rev.* 44 (2015) 8859–8876.
- [4] H. Zhang, Ultrathin two-dimensional nanomaterials, *ACS Nano* 9 (2015) 9451–9469.
- [5] D.H. Deng, K.S. Novoselov, Q. Fu, N.F. Zheng, Z.Q. Tian, X.H. Bao, Catalysis with two-dimensional materials and their heterostructures, *Nat. Nanotechnol.* 11 (2016) 218–230.
- [6] F. Bonaccorso, L. Colombo, G.H. Yu, M. Stoller, V. Tzozini, A.C. Ferrari, R.S. Ruoff, V. Pellegrini, Graphene, related two-dimensional crystals, and hybrid systems for energy conversion and storage, *Science* (80-) 347 (2015) 1246501.
- [7] J. Xu, Z.P. Wang, Y.F. Zhu, Enhanced visible-light-Driven photocatalytic disinfection performance and organic pollutant degradation activity of porous g-C<sub>3</sub>N<sub>4</sub> nanosheets, *ACS Appl. Mater. Interfaces* 9 (2017) 27727–27735.
- [8] W.Y. Lei, Y. Mi, R.J. Feng, P. Liu, S. Hu, J.G. Yu, X.F. Liu, J.A. Rodriguez, J.-o. Wang, L. Zheng, K. Tang, S.X. Zhu, G. Liu, M.H. Liu, Hybrid 0D–2D black phosphorus quantum dots–Graphitic carbon nitride nanosheets for efficient hydrogen evolution, *Nano Energy* 50 (2018) 552–561.
- [9] A.X. Yin, Q.Y. He, Z.Y. Lin, L. Luo, Y. Liu, S. Yang, H. Wu, M.N. Ding, Y. Huang, X.F. Duan, Plasmonic/Nonlinear optical material Core/Shell nanorods as nanoscale plasmon modulators and optical voltage sensors, *Angew. Chem. Int. Ed.* 55 (2016) 583–587.
- [10] J.Y. Shi, Y. Kuwahara, T.C. An, H. Yamashita, The fabrication of TiO<sub>2</sub> supported on slag-made calcium silicate as low-cost photocatalyst with high adsorption ability for the degradation of dye pollutants in water, *Catal. Today* 281 (2017) 21–28.
- [11] Y. Magatani, Y. Kuwahara, K. Nishizawa, H. Yamashita, Dramatically enhanced phenol degradation on alkali cation-anchored TiO<sub>2</sub>/SiO<sub>2</sub> hybrids: effect of cation- $\pi$  interaction as a diffusion-controlling tool in heterogeneous catalysis, *ChemistrySelect* 2 (2017) 4332–4337.
- [12] M. Che, K. Mori, H. Yamashita, Elaboration, characterization and properties of silica-based single-site heterogeneous photocatalysts, *Proc. R. Soc. A* 468 (2012) 2113–2128.
- [13] X.J. Bai, C.P. Sun, D. Liu, X.H. Luo, D. Li, J. Wang, N.X. Wang, X.J. Chang, R.L. Zong, Y.F. Zhu, Photocatalytic degradation of deoxynivalenol using Graphene/ZnO hybrids in aqueous suspension, *Appl. Catal. B: Environ.* 204 (2017) 11–20.
- [14] Y.B. Wang, X. Zhao, D. Cao, Y. Wang, Y.F. Zhu, Peroxymonosulfate enhanced visible light photocatalytic degradation bisphenol a by single-atom dispersed Ag mesoporous g-C<sub>3</sub>N<sub>4</sub> hybrid, *Appl. Catal. B: Environ.* 211 (2017) 79–88.
- [15] M.C. Wen, K. Mori, Y. Kuwahara, T.C. An, H. Yamashita, Design and architecture of metal organic frameworks for visible light enhanced hydrogen production, *Appl. Catal. B: Environ.* 218 (2017) 555–569.
- [16] Y.H. Sang, Z.H. Zhao, M.W. Zhao, P. Hao, Y.H. Leng, H. Liu, From UV to near-infrared, WS<sub>2</sub> nanosheet: a novel photocatalyst for full solar light Spectrum photodegradation, *Adv. Mater.* 27 (2015) 363–369.
- [17] G. Wang, B.B. Huang, X.C. Ma, Z.Y. Wang, X.Y. Qin, X.Y. Zhang, Y. Dai, M.H. Whangbo, Cu<sub>2</sub>(OH)PO<sub>4</sub>, a Near-Infrared-Activated Photocatalyst, *Angew. Chem. Int. Ed.* 52 (2013) 4810–4813.
- [18] M. Batmunkh, M. Bat-Erdene, J.G. Shapter, Phosphorene and phosphorene-based materials - prospects for future applications, *Adv. Mater.* 28 (2016) 8586–8617.
- [19] R. Gusmão, Z. Sofer, M. Pumera, Black phosphorus rediscovered: from bulk to monolayer, *Angew. Chem.* 129 (2017) 8164–8185.
- [20] W.Y. Lei, G. Liu, J. Zhang, M.H. Liu, Black phosphorus nanostructures: recent advances in hybridization, doping and functionalization, *Chem. Soc. Rev.* 46 (2017) 3492–3509.
- [21] L.K. Li, Y.J. Yu, G.J. Ye, Q.Q. Ge, X.D. Ou, H. Wu, D.L. Feng, X.H. Chen, Y.B. Zhang, Black phosphorus field-effect transistors, *Nat. Nanotechnol.* 9 (2014) 372–377.
- [22] M.Z. Rahman, C.W. Kwong, K. Davey, S.Z. Qiao, 2D phosphorene as a water splitting photocatalyst: fundamentals to applications, *Energy Environ. Sci.* 9 (2016) 709–728.
- [23] M.S. Zhu, Y. Osakada, S. Kim, M. Fujitsuka, T. Majima, Black phosphorus: a promising two dimensional visible and near-infrared-Activated photocatalyst for hydrogen evolution, *Appl. Catal. B: Environ.* 217 (2017) 285–292.
- [24] M.S. Zhu, C.Y. Zhai, M. Fujitsuka, T. Majima, Noble metal-free near-infrared-Driven photocatalyst for hydrogen production based on 2D hybrid of black Phosphorus/WS<sub>2</sub>, *Appl. Catal. B: Environ.* 221 (2018) 645–651.
- [25] J.R. Ran, B.C. Zhu, S.Z. Qiao, Phosphorene Co-catalyst advancing highly efficient visible-light photocatalytic hydrogen production, *Angew. Chem. Int. Ed.* 56 (2017) 10373–10377.
- [26] H.J.W. Jang, J.D.; Ryder, C.R.; Hersam, M.C.; Cahill, D.G., Anisotropic Thermal Conductivity of Exfoliated Black Phosphorus, *Adv. Mater.* 27 (2015) 8017–8022.
- [27] X.W. Wang, G.Z. Sun, N. Li, P. Chen, Quantum dots derived from two-dimensional materials and their applications for catalysis and energy, *Chem. Soc. Rev.* 45 (2016) 2239–2262.
- [28] R.S. Selinsky, Q. Ding, M.S. Faber, J.C. Wright, S. Jin, Quantum dot nanoscale heterostructures for solar energy conversion, *Chem. Soc. Rev.* 42 (2013) 2963–2985.
- [29] X. Zhang, H.M. Xie, Z.D. Liu, C.L. Tan, Z.M. Luo, H. Li, J.D. Lin, L.Q. Sun, W. Chen, Z.C. Xu, L.H. Xie, W. Huang, H. Zhang, Black phosphorus quantum dots, *Angew. Chem. Int. Ed.* 54 (2015) 3653–3657.
- [30] Z.B. Sun, H.H. Xie, S.Y. Tang, X.F. Yu, Z.N. Guo, J.D. Shao, H. Zhang, H. Huang, H.Y. Wang, P.K. Chu, Ultrasmall black phosphorus quantum dots: synthesis and use as photothermal agents, *Angew. Chem. Int. Ed.* 127 (2015) 11688–11692.
- [31] J.D. Shao, H.H. Xie, H. Huang, Z.B. Li, Z.B. Sun, Y.H. Xu, Q.L. Xiao, X.F. Yu, Y.T. Zhao, H. Zhang, H.Y. Wang, P.K. Chu, Biodegradable black phosphorus-based nanospheres for in vivo photothermal cancer therapy, *Nat. Commun.* 7 (2016) 12967.
- [32] K.F. Mak, C. Lee, J. Hone, J. Shan, T.F. Heinz, Atomically thin MoS<sub>2</sub>: a new direct-gap semiconductor, *Phys. Rev. Lett.* 105 (2010) 136805.
- [33] N.N. Meng, Y.F. Zhou, W.Y. Nie, P.P. Chen, Synthesis of CdS-Decorated RGO nanocomposites by reflux condensation method and its improved photocatalytic activity, *J. Nanopart. Res.* 18 (2016) 241.
- [34] T. Hong, B. Chamlagain, T.J. Wang, H.J. Chuang, Z.X. Zhou, Y.Q. Xu, Anisotropic photocurrent response at black Phosphorus-MoS<sub>2</sub> p-n heterojunctions, *Nanoscale* 7 (2015) 18537–18541.
- [35] R. He, J. Hua, A.Q. Zhang, C.H. Wang, J.Y. Peng, W.J. Chen, J. Zeng, Molybdenum disulfide-black phosphorus hybrid nanosheets as a superior catalyst for electrochemical hydrogen evolution, *Nano Lett.* 17 (2017) 4311–4316.
- [36] U. Gupta, C.N.R. Rao, Hydrogen generation by water splitting using MoS<sub>2</sub> and other transition metal dichalcogenides, *Nano Energy* 41 (2017) 49–65.
- [37] W.Y. Lei, T.T. Zhang, P. Liu, J.A. Rodriguez, G. Liu, M.H. Liu, Bandgap and local field-dependent photoactivity of Ag-Black phosphorus nanohybrids, *ACS Catal.* 6 (2016) 8009–8020.
- [38] A. Favron, E. Gaufres, F. Fossard, A.L. Phaneuf-L'Heureux, N.Y.W. Tang, P.L. Levesque, A. Loiseau, R. Leonelli, S. Francoeur, R. Martel, Photooxidation and quantum confinement effects in exfoliated black phosphorus, *Nat. Mater.* 14 (2015) 826–833.
- [39] Y. Mi, Z. Zhang, L. Zhao, S. Zhang, J. Chen, Q. Ji, J. Shi, X. Zhou, R. Wang, J. Shi, W. Du, Z. Wu, X. Qiu, Q. Zhang, Y. Zhang, X. Liu, Tuning excitonic properties of monolayer MoS<sub>2</sub> with microsphere cavity by high-throughput chemical vapor deposition method, *Small* 13 (2017) 1701694.
- [40] C. Mai, A. Barrette, Y.F. Yu, Y.G. Semenov, K.W. Kim, L.Y. Cao, K. Gundogdu, Many-body effects in Valleytronics: direct measurement of valley lifetimes in single-layer MoS<sub>2</sub>, *Nano Lett.* 14 (2014) 202–206.
- [41] Y.G. Li, H.L. Wang, L.M. Xie, Y.Y. Liang, G.S. Hong, H.J. Dai, MoS<sub>2</sub> nanoparticles grown on graphene: an advanced catalyst for the hydrogen evolution reaction, *J. Am. Chem. Soc.* 133 (2011) 7296–7299.
- [42] G.J. Guan, S.Y. Zhang, S.H. Liu, Y.Q. Cai, M. Low, C.P. Teng, I.Y. Phang, Y. Cheng, K.L. Duei, B.M. Srinivasan, Y.G. Zheng, Y.W. Zhang, M.Y. Han, Protein induces layer-by-layer exfoliation of transition metal dichalcogenides, *J. Am. Chem. Soc.* 137 (2015) 6152–6155.
- [43] J.A. Wilson, A.D. Yoffe, Transition metal dichalcogenides discussion and interpretation of observed optical, electrical and structural properties, *Adv. Phys.* 18 (1969) 193–335.
- [44] J.P. Wilcoxon, G.A. Samara, Strong quantum-size effects in a layered semiconductor - MoS<sub>2</sub> nanoclusters, *Phys. Rev. B* 51 (1995) 7299–7302.
- [45] Y.Y. Huang, Y.J. Chen, C.L. Hu, B. Zhang, T. Shen, X.D. Chen, M.Q. Zhang, 'Bridge' effect of CdS nanoparticles in the interface of graphene-polyaniline composites, *J. Mater. Chem.* 22 (2012) 10999–11002.
- [46] X. Zong, Z. Xing, H. Yu, Y. Bai, G.Q. Lu, L.Z. Wang, Photocatalytic hydrogen production in a noble-metal-free system catalyzed by in situ grown molybdenum

- sulfide catalyst, *J. Catal.* 310 (2014) 51–56.
- [47] Z.B. Chen, D. Cummins, B.N. Reinecke, E. Clark, M.K. Sunkara, T.F. Jaramillo, Core-shell  $\text{MoO}_3\text{-MoS}_2$  nanowires for hydrogen evolution: a functional design for electrocatalytic materials, *Nano Lett.* 11 (2011) 4168–4175.
- [48] J. Zhang, T. Wang, D. Pohl, B. Rellinghaus, R. Dong, S. Liu, X. Zhuang, X. Feng, Interface engineering of  $\text{MoS}_2/\text{Ni}_3\text{S}_2$  heterostructures for highly enhanced electrochemical overall-water-splitting activity, *Angew. Chem. Int. Ed.* 55 (2016) 6702–6707.
- [49] J.G. Chen, NEXAFS investigations of transition metal oxides, Nitrides, carbides, sulfides and other interstitial compounds, *Surf. Sci. Rep.* 30 (1997) 1–152.
- [50] M.S. Zhu, S. Kim, L. Mao, M. Fujitsuka, J.Y. Zhang, X.C. Wang, T. Majima, Metal-free photocatalyst for  $\text{H}_2$  evolution in visible to near-infrared region: black Phosphorus/Graphitic carbon nitride, *J. Am. Chem. Soc.* 139 (2017) 13234–13242.
- [51] X.D. Zhang, X. Xie, H. Wang, J.J. Zhang, B.C. Pan, Y. Xie, Enhanced photo-responsive ultrathin graphitic-phase  $\text{C}_3\text{N}_4$  nanosheets for bioimaging, *J. Am. Chem. Soc.* 135 (2013) 18–21.
- [52] M.B. Price, J. Butkus, T.C. Jellicoe, A. Sadhanala, A. Briane, J.E. Halpert, K. Broch, J.M. Hodgkiss, R.H. Friend, F. Deschler, Hot-carrier cooling and photoinduced refractive index changes in organic-inorganic lead halide perovskites, *Nat. Commun.* 6 (2015) 8420.
- [53] D.B. Velusamy, M.A. Haque, M.R. Parida, F. Zhang, T. Wu, O.F. Mohammed, H.N. Alshareef, 2D organic-inorganic hybrid thin films for flexible UV-Visible photodetectors, *Adv. Funct. Mater.* 27 (2017) 1605554.
- [54] H. Tong, S.X. Ouyang, Y.P. Bi, N. Umezawa, M. Oshikiri, J.H. Ye, Nano-photo-catalytic materials: possibilities and challenges, *Adv. Mater.* 24 (2012) 229–251.
- [55] J. Liu, Y. Liu, N.Y. Liu, Y.Z. Han, X. Zhang, H. Huang, Y. Lifshitz, S.-T. Lee, J. Zhong, Z.H. Kang, Metal-free efficient photocatalyst for stable visible water splitting via a two-electron pathway, *Science* (80-) 347 (2016) 970–974.
- [56] H. Vovusha, B. Sanyal, Adsorption of Nucleobases on 2D transition-metal dichalcogenides and graphene sheet: a first principles density functional theory study, *RSC Adv.* 5 (2015) 67427–67434.
- [57] M. Ou, Q. Zhong, S.L. Zhang, L.M. Yu, Ultrasound assisted synthesis of heterogeneous  $\text{g-C}_3\text{N}_4/\text{BiVO}_4$  composites and their visible-light-induced photocatalytic oxidation of NO in gas phase, *J. Alloy. Compd.* 626 (2015) 401–409.
- [58] Y.M. He, L.H. Zhang, B.T. Teng, M.H. Fan, New application of Z-Scheme  $\text{Ag}_3\text{PO}_4/\text{g-C}_3\text{N}_4$  composite in converting  $\text{CO}_2$  to fuel, *Environ. Sci. Technol.* 49 (2015) 649–656.